View metadata, citation and similar papers at core.ac.uk
brought to you by CORE
provided by Ghent University Academic Bibliography

Check for updates

OSA CONTINUUM

Compact silicon photonics circuit to extract multiple parameters for process control monitoring

YUFEI XING,[1,2,*] MI WANG,[1,2] ALFONSO RUOCCO,[1,2,3] JORIS GEESSELS,[4] UMAR KHAN,[1,2] AND WIM BOGAERTS[1,2]

[1] *Photonics Research Group, Ghent University-IMEC, Ghent, Belgium*
[2] *Center of Nano and Biophotonics, Ghent, Belgium*
[3] *Currently at Cambridge Graphene Centre, Cambridge University, Cambridge, UK*
[4] *Luceda Photonics, Dendermonde, Belgium*
[*] *yufei.xing@ugent.be*
http://photonics.intec.ugent.be/contact/people.asp?ID=332

Abstract: We present a compact interferometer circuit to extract multiple model parameters of on-chip waveguides and directional couplers from optical measurements. The compact design greatly improves the accuracy of extraction with fewer measurements, making it useful for process monitoring and detailed wafer-level variability analysis. We discuss the design requirements and illustrate the extraction using the Restart-CMA-ES global optimization algorithm.

© 2020 Optical Society of America under the terms of the OSA Open Access Publishing Agreement

1. Introduction

Silicon Photonics is one of the key photonic technologies for large-scale integration. The high material index contrast and strong light confinement help in achieving high integration density, but they also make circuits very susceptible to process variations. The variations in fabricated waveguide width and thickness result into deviations from the desired optical properties, such as the effective and group indices of guided waveguide modes or coupling coefficients in *directional couplers* (DC). As circuits become larger, component performance deviations will propagate and accumulate, causing performance degradation and lower fabrication yield of optical circuits, and especially of interferometric circuits like wavelength filters.

With variability analysis, we want to link the fabrication variations to performance variations of larger circuits. It involves performance evaluation [1], variability modeling [2], yield prediction [3], and ultimately optimization of circuits for robustness [4]. For these studies, it is essential to perform *process control monitoring* (PCM) where the essential properties and variations of the fabrication process are monitored. PCM extracts technology specific parameters across a wafer (and between wafers and fabrication lots) that become the input data for device-level and circuit-level variability analysis [5]. The devices or circuits for parameter extraction should be compact so they can be placed at various locations without disturbing the layout of the actual functional circuits, but still allow to construct a granular map of the process variation on the fabricated chips. This then serves as input for location-dependent variability analysis and yield prediction of future designs.

For submicrometer silicon photonic waveguides, the fabricated linewidth and thickness are two fundamental parameters to monitor. Nowadays, foundries often offer linewidth metrology measurements based on top-down *Scanning Electron Microscopy* (SEM). This method is time-consuming and can only be performed when the waveguides are still exposed, so any changes induced by processing steps later in the fabrication flow are not taken into account. Cross-section SEM inspections can be more representative, but this is a destructive process. Alternative methods are ellipsometry and scatterometry, which are non-destructive but are also performed

#383711 https://doi.org/10.1364/OSAC.383711
Journal © 2020 Received 19 Nov 2019; revised 29 Jan 2020; accepted 4 Feb 2020; published 14 Feb 2020

early in the process flow, as the addition of many layers in the back-end-of-line metallization stack complicates the measurement. These direct measurement techniques typically have a precision of a few nanometers [6]. In high-contrast waveguides where nm-scale geometry deviations have a non-negligible effect on the propagation constant, this precision is not sufficient. Therefore, for variability analysis, we preferably measure parameters on the final fabricated circuits and over a large number of sites to obtain the variability contributions at different length scales.

Therefore, optical transmission measurements provide a very attractive alternative to measure fabricated geometry. *Mach-Zehnder interferometers* (MZIs) and ring resonators can be used to extract the average effective and group indices of the guided waveguide mode along the path of a delay line [7–12]. Because silicon waveguides are extremely sensitive to geometry variations, the effective and group indices can be mapped onto geometric parameters such as waveguide linewidth and thickness, which allows us to derive small variations in the fabricated waveguide geometry. By placing many copies of such test circuits over the wafer and automating wafer-scale optical transmission measurements, we can obtain a detailed wafer map of fabricated waveguide geometry with a sub-nanometer accuracy [12].

The method proposed in [8] uses a ring resonator which consists of both straight and bent waveguides. Since straight and bent waveguides have different effective and group indices of the guided mode, the geometrical cross-section of a straight waveguide cannot be extracted accurately from a ring, without making assumptions on the correlation between straight and bend geometry that are difficult to verify. In [7] and [12], we used a combination of a low and a high order MZI to extract the effective index n_{eff} and group index n_g of the fundamental TE mode of straight silicon waveguides. The fabrication variation can shift the transmission spectrum of an MZI by more than one *free spectral range* (FSR), making it difficult to identify the correct discrete interference order, resulting into multiple solutions for the effective index n_{eff}. So, we designed the order of one MZI sufficiently low, such that its spectrum will not shift more than one FSR under the expected process variation [12]. This low-order MZI offers a local reference for the effective index. The second, high-order MZI has many more interference orders within the measurement range, offering more spectral features for accurate extraction of both effective and group indices. The order of the high-order MZI is designed such that we can still estimate the effective index reliably based on the local reference effective index extracted from the low-order MZI.

In addition to waveguide parameters, the parameters of a DC are also essential in the performance of many optical filters, such as MZI or ring-based lattice filters. A common method to characterize the properties of the directional coupler is to measure the power transmission of at least two DCs (and preferably 3 or more) with different coupling length, in order to separate the length-dependent coupling and the contribution of the bends [13]. And to eliminate the effect of the wavelength dependent coupling efficiency of the *grating couplers* (GC) used for the measurement, we measure the two outputs of the directional coupler and normalize the transmission to the total power. Therefore, in total, 3 DCs and 6 optical measurements are required for the extraction of coupler parameters, and even then we have to assume that the properties of these three DCs are identical. Any variation in linewidth, thickness, and gap among the DCs will introduce extraction errors. Therefore, it is desirable to bring the three DCs as closely together on the chip to reduce the extraction error caused by the local variations.

There are two major challenges in the current designs of the monitoring circuits we originally proposed in [12]. First, the footprint of the monitoring circuit(s) needs to be reduced significantly. A compact monitoring circuit reduces local variation within the circuit, which improves extraction accuracy and takes up less space that can be then be used for functional circuits. In the two-MZI design for the extraction of the effective index $\mathrm{n_{eff}}$ and the group index $\mathrm{n_g}$ of of thefundamental TE mode of a silicon waveguide (Fig. 1(b)), we assumed that the two MZIs are on the same location on the die and they only suffer random device-to-device variation between them. In

OSA CONTINUUM

the design to extract the DC parameters (Fig. 1(c)), we assumed that the DCs in the three MZIs experience the same fabrication variation so that they have identical cross-section and bend geometry. Such assumptions are less convincing when the monitoring circuit is not compact, as it becomes plausible that different sites within the circuit suffer significantly different linewidth and thickness variations. Besides, process variations can have a significant deterministic contribution that can be determined by its location on a wafer [2]. As a result, the fabrication variation is correlated between nearby sites. For example, on the intra-die level, linewidths are correlated within a range of several hundreds of micrometers because of the averaging of local pattern density effects. To extract the detailed location dependencies of the deterministic variation and to observe such a short-distance spatial correlation, we need to design the monitoring circuit as compact as possible. The small footprint has the added benefit of making it easy to squeeze many copies of the monitor circuit in various locations around and within the functional designs, very close to the regions of interest.

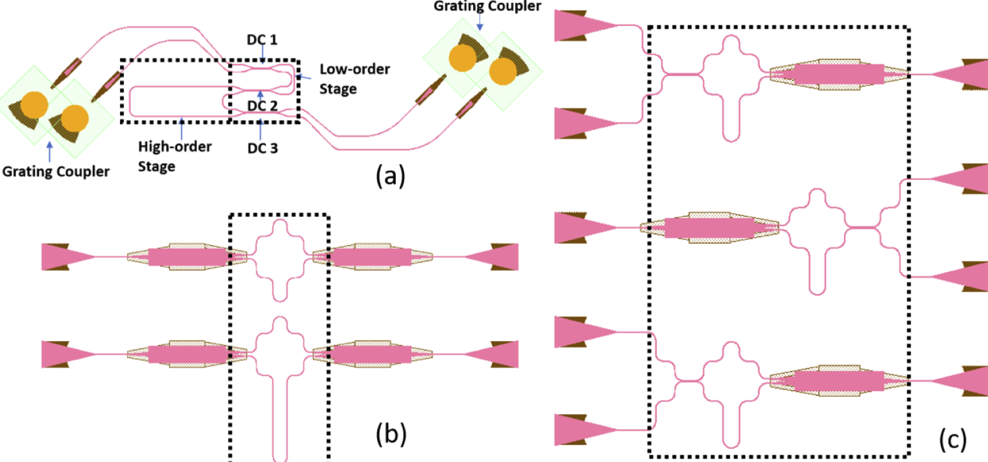

Fig. 1. (a) The layout of the folded two-stage MZI. The circuit has two MZI stages connected by three DCs with an identical cross section for the straight coupling section and identical bends. We used low-reflection GCs [14] to reduce measurement noise due to parasitic back-reflections. The circuit has a compact footprint of 400 μm $\times$ 100 μm. The large dotted frame indicates the region to extract process variation of the waveguide, and it covers an area of 120 μm $\times$ 40 μm. The small dotted frame on the right indicates the region to extract process variation in the DC, and it covers three DCs with an area of 45 μm $\times$ 40 μm. (b) The layout of the two MZIs to extract waveguide parameters used in [12]. The design has a footprint of 350 μm $\times$ 180 μm. The region to extract process variations in the waveguide covers an area of 55 μm $\times$ 180 μm. (c) The layout of the three MZIs to extract DC parameter used in [13]. The design has a footprint of 285 μm $\times$ 280 μm. The region to extract process variation in the DC covers an area of 150 μm $\times$ 220 μm.

The second challenge is the significant time needed for the optical measurement of the process monitoring circuits, especially when we need to extract parameters from multiple circuits. The measurement time becomes substantial when we are collecting a detailed wafer map, as the number of sites can easily run into the hundreds or thousands: if each die requires 100 monitoring circuits, a wafer would easily contain many thousands of such circuits. Each fiber-to-fiber measurement requires an alignment step onto the grating couplers and a high-resolution wavelength sweep. These steps can be optimized, but still a single transmission measurement can easily take 30 seconds. Therefore, the automated measurement on all circuits on a wafer would take days or even weeks. In particular, when using separate circuits to extract waveguide parameters and DC

parameters, already 8 measurements are needed per site. If we could reduce the number of optical measurements for each monitoring circuit, we will significantly reduce the measurement time.

2. Design of the monitoring circuit

To reduce the footprint of test structures and the number of optical measurements for performance evaluation, we present in this paper a two-stage MZI design, shown in Fig. 1(a), with which we can simultaneously extract effective and group indices of a waveguide mode and the parameters of the used DCs. The design wraps the low-order and high-order MZI into one circuit with two inputs and two outputs. Including low-reflection GCs [14], the entire circuit has a footprint of 400 μm $\times$ 100 μm which could be further reduced by adjustment of the layout.

The region to extract process variation in the waveguide includes the arms of both the low-order stage and the high-order stage. It covers an area of 120 μm $\times$ 40 μm. It is 1.6$\times$ smaller in terms of footprint and 2.1$\times$ smaller in terms of the region to extract variation compared to the two-MZI design in Fig. 1(b) which we used in [12] for waveguide parameter extraction. For DC parameter extraction, the region of interest is the small rectangle that covers three DCs with an area of 45 μm $\times$ 40 μm. Our monitoring circuit is 2.0$\times$ smaller in terms of footprint and 18.3$\times$ smaller in terms of the region to extract variation compared to the three-MZI design in Fig. 1(c) used in [13]. The design is organized to be very compact which reduces the local variation between waveguides and DCs, which in turn improves extraction accuracy. Moreover, the circuit requires only 2 optical measurements instead of 8 to extract all waveguide and DC parameters, which significantly reduces the cost of the automated optical measurements.

We design the two-stage MZI using the same rules for the low and high order as described in [12]. The total process variation on an isolated waveguide on SOI platform, which includes wafer-to-wafer, die-to-die, intra-die variations, . . . be quite large [15]. For instance, linewidths between two different points on two different wafers from two different fabrication lots can differ as much as 10-20 nm. Variations that originate at levels such as lot-to-lot, wafer-to-wafer, and die-to-die variations have the same impact on every device in a die. As illustrated in [15], we categorize these variations together as the inter-die variation. On top of that, we get the intra-die variation that affects devices differently on the same die, which can be further decomposed into location-dependent variation and local variation. These variations are much smaller than the variations between lots, wafers and dies on the same wafer. The location-dependent variation depends on the position of the circuit with respect to the center or edge of the die, but also on the environment of the circuit, and especially the surrounding pattern density. On the other hand, the local variation we define here induces local disparities between devices placed close together (less than a few hundred microns apart). It includes residual random fluctuations of thickness and waveguide width. The sum of these three variations gives us the total process variation of a device.

$$variation_{total} = variation_{inter-die} + variation_{location-dependent} + variation_{local} \tag{1}$$

With the two-stage MZI, we address variations on the different levels in three steps. The first step, we extract the effective index n_{eff} of the waveguide mode from a low-order stage. Without prior accurate information on the group index n_g extracted from the low-order stage, we can estimate the range of n_{eff}

$$\Delta n_{eff,total} = \frac{\partial n_{eff}}{\partial w}\Delta w_{total} + \frac{\partial n_{eff}}{\partial t}\Delta t_{total} \tag{2}$$

In the second step, we obtain an n_{eff} map over the die by interpolation, where we can remove the local variation, and the inter-die variation and location-dependent variation together determines the average value. In the third step, we use an interpolated value of $n_{eff,low}$ at each location as a reference. Now, rather than the total variation we only need to deal with the much smaller local

OSA CONTINUUM

variation. Since we can accurately extract n_g on the high-order stage, the range for n_{eff} under the local variation is estimated by substituting geometry variation using the local variation as defined in Eq. (12) in Ref. [12].

$$\Delta n_{eff,local} = \left(-\frac{\frac{\partial n_{eff}}{\partial w}\frac{\partial n_g}{\partial t}}{\frac{\partial n_g}{\partial w}} + \frac{\partial n_{eff}}{\partial t} \right) \Delta t_{local} \tag{3}$$

We based our designs on the specifications in IMEC's technology handbook for the iSiPP50G silicon photonics platform. For the waveguides, the standard deviation in linewidth is specified as 5.3 nm over the wafer, while the thickness has a standard deviation of 0.7 nm. For a safe design based on a 6σ spread, we targeted waveguides of 470±15 nm line width and 210±5 nm thickness, which give the range of the total variation. We made an approximation in our model by assuming that the waveguide is rectangular with a 90° sidewall, where in reality the sidewall angle is specified to be larger than 85°, so it is not necessarily vertical. As we are mostly interested in relative variations on the wafer and between wafers, this deviation from the vertical is not a major issue, and if necessary the model could be expanded to incorporate the sidewall angle. Without prior information of of the group index n_g in the low-order stage, we can estimate the tolerance of its n_{eff} by Eq. (2):

$$\begin{aligned}\Delta n_{eff,total} &= \frac{\partial n_{eff}}{\partial w}\Delta w_{total} + \frac{\partial n_{eff}}{\partial t}\Delta t_{total} \\ &= 0.0019 \text{ nm}^{-1} \times 30 \text{ nm} + 0.0040 \text{ nm}^{-1} \times 10 \text{ nm} = 0.097.\end{aligned} \tag{4}$$

This then allows us to calculate the maximum delay length for the low-order MZI tat would still allow us to unambiguously calculate n_{eff}. With the above numbers, this amounts to a value of $L_{low\ order} < \frac{\lambda}{\Delta n_{eff,total}} = 16.0\mu$m. We estimate the local variation from the maximum difference between an extracted parameter with an interpolated wafer map. Based on Eq. (3):

$$\Delta n_{eff,local} = 0.0064 \text{ nm}^{-1} \times 0.8 \text{ nm} \times 2 = 0.0102, \tag{5}$$

We also know that thickness varies smoothly over the wafer, with local variations on two measured dies smaller than ± 0.6 nm [12]. So here we assume the maximum local variation (within the MZI circuit) is below ±0.8 nm. Local width variation can be as large as 4 nm. As analyzed in [12], when the width variation is significantly larger than the thickness variation, that $\Delta w > -\frac{\partial w}{\partial n_g} \cdot \frac{\partial n_g}{\partial t}\Delta t$, the range of n_{eff} is determined by Δt. In the high-order MZI, the extraction of n_g is much more accurate, as we cover more interference orders in the measurement range. For $w \in [455,485]$ nm and $t \in [205,215]$ nm, we can now, knowing the accurate local n_g, estimate the range of the high-order n_{eff} by Eq. (3).

Then $L_{high\ order} < \lambda/\Delta n_{eff,local} = 152.0\mu$m. From the above analysis, we choose the arm length difference of the low-order stage as 15 μm and the high-order as 150 μm.

To extract DC parameters, we put three DCs with different length connecting the two MZI stages, and the coupler lengths correspond to a nominal 25%, 50%, 75% cross coupling power at 1550 nm. The gap between the waveguides in the DC is 250 nm, and the corresponding coupler length in three DCs are 6.65 μm, 12.91 μm, 19.17 μm. To further reduce the footprint of the device, we also folded the MZI as shown in Fig. 1(a) so that we shorten the distance between the pairs of arms and the three DCs. This design should reduce local variation and improve extraction accuracy.

3. Extracting multiple parameters using the restart-CMA-ES method

We extract the parameters of the folded MZI circuits by matching a simulated spectrum with the measured spectrum. This requires a behavioral model for the circuit (and its constituent components). As in Fig. 2, for a waveguide arm of the MZI, we use two compact model parameters, namely the effective index n_{eff} and the group index n_g of TE mode at $\lambda_0 = 1550$ nm. The effective index n_{eff} at a given wavelength is then:

$$n_{eff}(\lambda) = n_{eff} - (\lambda - \lambda_0) \cdot \frac{n_g - n_{eff}}{\lambda_0} \tag{6}$$

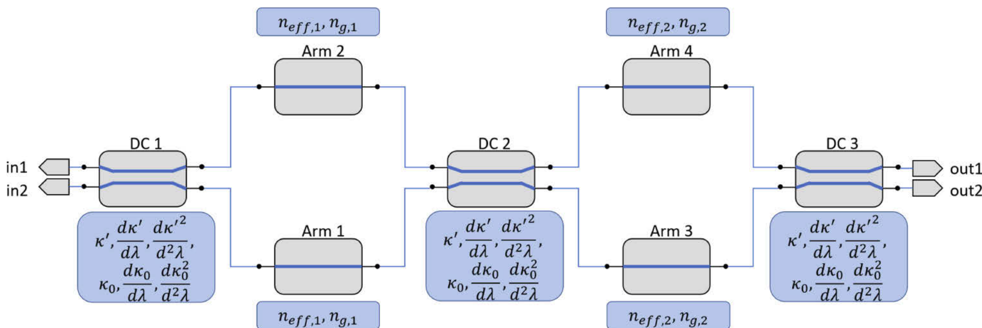

Fig. 2. The circuit model of the device. Two MZI stages have different n_{eff} and n_g led by the local fabrication variation.

Even with a small circuit like this, local fabrication variations within the circuit could make the width and thickness differ in the two arms of the same stage. In addition, the width and thickness on the same arm can vary along the waveguide. Therefore, the extracted effective index and mapped width from the spectral measurements are averaged over the two waveguides within the same stage. As it is impossible to separate the effective indices of the two arms in the same stage, we only fit a single value of n_{eff} in each stage of the MZI. We do choose different effective index parameters for the two stages. In the high-order stage, the long arm is significantly longer than the shorter arm, so the extracted width is mostly determined by the long arm. Comparing the layout, the effective index of the low and high order stage are likely to suffer somewhat different variations because the two stages have a different footprint. This is another argument why it is reasonable to assume different average effective index values for the two stages in the circuit model.

A DC gets coupling contribution from two parts: the straight coupling section and its two bends [13]. When we neglect insertion loss, the power at the cross-coupled port is:

$$K_{coupled}(\lambda) = sin^2(\kappa'(\lambda)L_{coupler} + \kappa_0(\lambda)) \tag{7}$$

The DC model we use here has six parameters, namely the length-specific coupling coefficient of the straight coupling part κ' and its first and second-order derivative with wavelength $\partial\kappa'/\partial\lambda$ and $\partial^2\kappa'/\partial\lambda^2$, and the lumped power coupling of the bend κ_0 and again its first and second-order derivative $\partial\kappa_0/\partial\lambda$ and $\partial^2\kappa_0/\partial\lambda^2$.

$$\kappa'(\lambda) = \kappa'(\lambda_0) + (\lambda - \lambda_0)\frac{\partial\kappa'}{\partial\lambda}(\lambda_0) + \frac{1}{2}(\lambda - \lambda_0)^2\frac{\partial^2\kappa'}{\partial\lambda^2}(\lambda_0) \tag{8}$$

$$\kappa_0(\lambda) = \kappa_0 + (\lambda - \lambda_0)\frac{\partial\kappa_0}{\partial\lambda}(\lambda_0) + \frac{1}{2}(\lambda - \lambda_0)^2\frac{\partial^2\kappa_0}{\partial\lambda^2}(\lambda_0) \tag{9}$$

We implemented the compact model of the two-stage MZI in the IPKISS circuit simulator CAPHE of Luceda Photonics [16]. We then try to match the simulated spectrum to the measured optical

OSA CONTINUUM

spectrum by adjusting the model parameters. To remove the effect of GCs in the spectrum, we measured both the spectra from port *in1* to *out1* and *in1* to out2 and normalized the transmission spectra to the sum of the two spectra. The solid red curve in Fig. 3 shows a typical normalized measured spectrum from port *in1* to port *out1*.

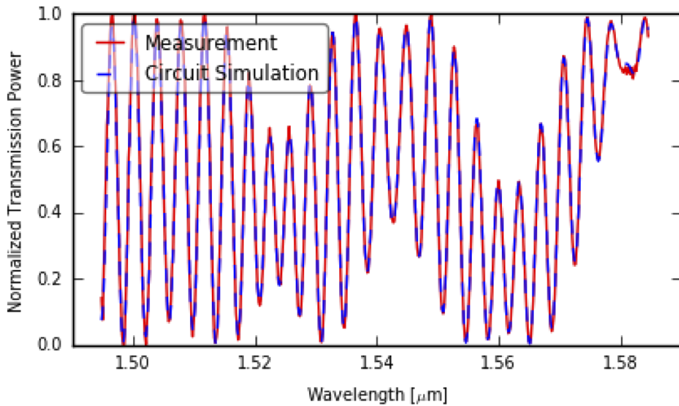

Fig. 3. A good match between simulated and measured spectra is achieved by the restart-CMA-ES method. Red: measured spectrum. Blue: simulated spectrum by CAPHE.

Standard curve fitting methods (e.g. from the scientific python package 'scipy') are capable of extracting parameters from a single MZI response [12]. However, it becomes difficult to use these curve fitting algorithms to extract parameters from the two-stage MZI. As shown in Fig. 3, the spectrum of the device is more complicated. We are not interested in a local minimum in the difference between the simulated and measured spectrum. However, the classical curve-fitting methods fail to handle the non-convex parameter landscape and will converge to a local solution instead of the global optimum.

Instead, we can use smart global optimization algorithms that adaptively choose the samples to drastically reduce the number of simulations for the non-convex parameter landscape optimization. Covariance Matrix Adaptation Evolutionary Strategy (CMA-ES) is an optimization method that adaptively chooses its searching path and searching range. The algorithm decides samples of the population of a new generation based on the samples offering the best optimization of the previous generation [17]. The CMA-ES dramatically reduces the sample number in the extraction and is especially powerful to extract multiple parameters simultaneously. Also, unlike other optimization technique, it has only a few parameters to set up, which is easy and intuitive to use. The method has been implemented in many programming languages, and the source code is accessible from [18]. The technique is also suitable when we apply it to extract a spectrum with complex features, but it does not guarantee always to find the global optimum. A variation, the Restart-CMA-ES method, is a global optimization method which is suitable for our purpose. In particular, we adopted the method described in [19]. We decide that the optimization reaches the global optimum when the objective function is below a predefined value. We restart the CMA-ES search if the method only obtains a local optimum. After each restart, we increase the population size, so the search characteristic becomes more global after each restart. The loop stops when the difference between the simulation and measurement is below the defined threshold, which indicates that the global optimum is obtained. We validated the algorithm with simulated samples with ±0.2 dB (5%) intensity noise to emulate the typical "measurement noise". The noise level is estimated from a large number of wafer-scale measurements. The measured 'noise' on our transmission spectra includes unwanted spectral fringes induced by scattering and back-coupling in the circuit, detector noise, etc. The optimization algorithm works robustly for

OSA CONTINUUM

simulated spectra with a noise corresponding to a large waveguide variation (w∈[465,485] nm, t∈[205,215] nm) and DC gap ∈[100,400] nm. Later, we also applied the method and successfully derived the optimal fitting for all 5841 circuit transmissions measured over the wafer, which proves the method is very robust for wafer-scale parameter extraction.

As shown in Fig. 3, we obtain an excellent matching between simulated and measured spectra using the restart-CMA-ES with increasing population after each restart. To extract ten parameters with high accuracy, usually, the optimization requires less than 20,000 iterations. The behavior parameters have been extracted with excellent accuracy (Table 1). The fitting uncertainty we presented is the estimate of 2× the standard deviations of each of the parameters, which provides confidence limits of approximately 95%. The fitting uncertainty for the parameters of the fundamental TE mode of the waveguide $n_{eff,2}$ is 2.3×10^{-7}, and the fitting uncertainty for $n_{g,2}$ is 2.1×10^{-5}. These fitting uncertainties propagate to fitting uncertainties of 0.01 nm in both width and thickness.

Then, we mapped the width and thickness of the high-order stage arm from $n_{eff,2}$ and $n_{g,2}$ (Table 2). As explained in [12], the extraction of geometry parameters includes several sources of uncertainties and errors, i.e. the model, the simulations, the mapping, and the fitting procedure. The modeling error is the mismatch between the compact circuit model and the actual fabricated circuit behavior; for example, assuming identical parameters κ' and κ_0 for the three DCs while the fabricated DCs have some disparity. The simulation error is the difference between the actual waveguide geometry (the shape, dimension and material properties) and the rectangular geometry we used in the mode solver. This error is hard to compensate, but its effects are largely relative and will not affect the trends in the extracted parameters. The mapping error is the difference between the simulated waveguide geometry and extracted waveguide geometry. The mapping error of width and thickness are 0.06 nm and 0.08 nm respectively, when we apply a third-order polynomial fitted model. The fitting uncertainty is estimated by twice the standard deviation of each parameter obtained by the fitting, which provides confidence limits of approximately 95%. Extracted width and thickness each have a 0.01 nm fitting uncertainty (Table 3).

Table 1. Obtained parameter values from spectral measurement and fitting uncertainties using the Restart CMA-ES method.

	Obtained Value	Fitting Uncertainty		Obtained Value	Fitting Uncertainty
$n_{eff,1}$	2.356	1.456e-6	$\frac{d\kappa'}{d\lambda}$	2.149e-1	9.147e-5
$n_{g,1}$	4.228	1.322e-4	$\frac{d\kappa'^2}{d^2\lambda}$	1.990	4.060
$n_{eff,2}$	2.356	2.284e-7	κ_0	2.315e-1	7.852e-5
$n_{g,2}$	4.220	2.105e-5	$\frac{d\kappa_0}{d\lambda}$	1.438	1.266e-2
κ'	4.173e-2	5.863e-6	$\frac{d\kappa_0^2}{d^2\lambda}$	8.110e-1	6.325e-2

Table 2. Extracted waveguide width and thickness of the high-order stage arm.

Parameter	Extracted Value	Fitting Uncertainty	Mapping Error	Total Error and Uncertainty
Width	474.68 nm	0.01 nm	0.06 nm	0.07 nm
Thickness	208.35 nm	0.01 nm	0.08 nm	0.09 nm

OSA CONTINUUM

Table 3. Statistics of measured width and thickness.

	Width	Thickness
Mean [nm]	464.7	210.3
Standard Deviation [nm]	4.6	0.8
Max [nm]	476.0	214.3
Min [nm]	450.8	208.4
Max-Min [nm]	25.2	5.9

4. Results

We put our monitoring circuit on a 200 mm wafer fabricated by IMEC's passive silicon photonics platform, accessed through the Europractice multi-project-wafer (MPW) service. The devices are patterned in an SOI wafer with 220 nm starting silicon thickness, using 193 nm lithography. The test circuits are interspersed on a larger design, which itself only occupies part of the illumination field of the reticle, as it is combined with the designs of other participants in the MPW run. As such, we cannot perform measurements uniformly over the wafer, but only on the die areas where our own design is located.

We first automated the optical measurements on 117 copies of the two-stage MZI on the same die (Fig. 4(a)) in the center of the wafer. These measurements were performed using a calibrated laser in a clean room environment with the temperature controlled at 20 degree Celsius. the light from the fiber is coupled to the chip using grating couplers that selectively couple to the fundamental TE mode of the waveguide, and coupled out through similar grating couplers

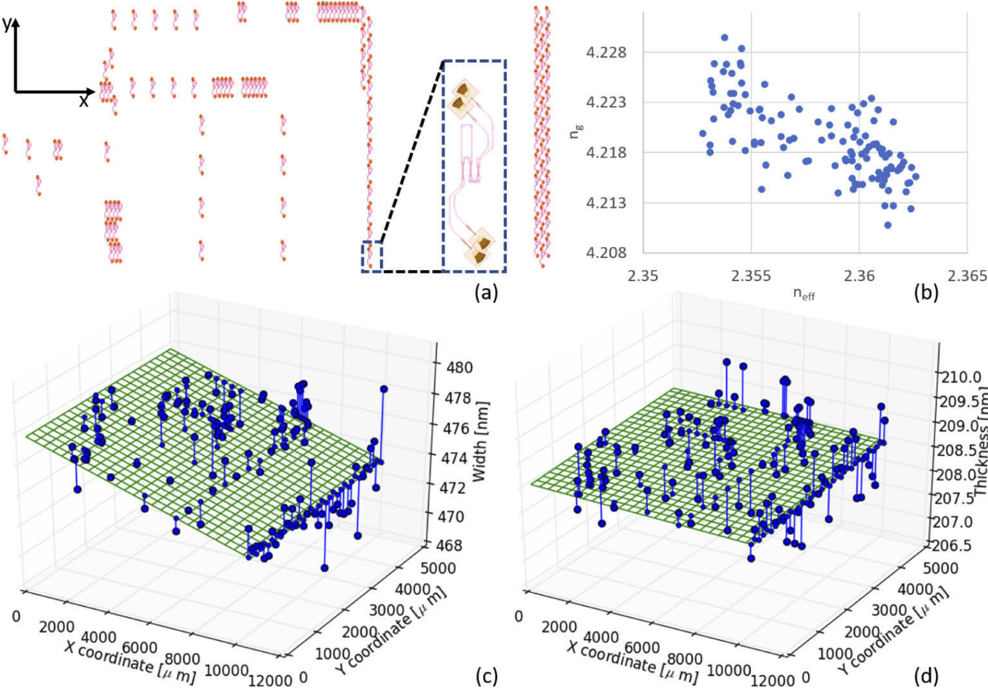

Fig. 4. (a) Locations of the folded two-stage MZIs on a die. (b) Extracted $n_{eff,2}$ and $n_{g,2}$ of die (X=0, Y=0) (in the center of the wafer). (c) Extracted width map and (d) thickness map of the die. x and y indicate the locations of the MZIs on the die. Blue dots: extracted value. Green grid: fitted map of extracted values using a linear function.

OSA CONTINUUM

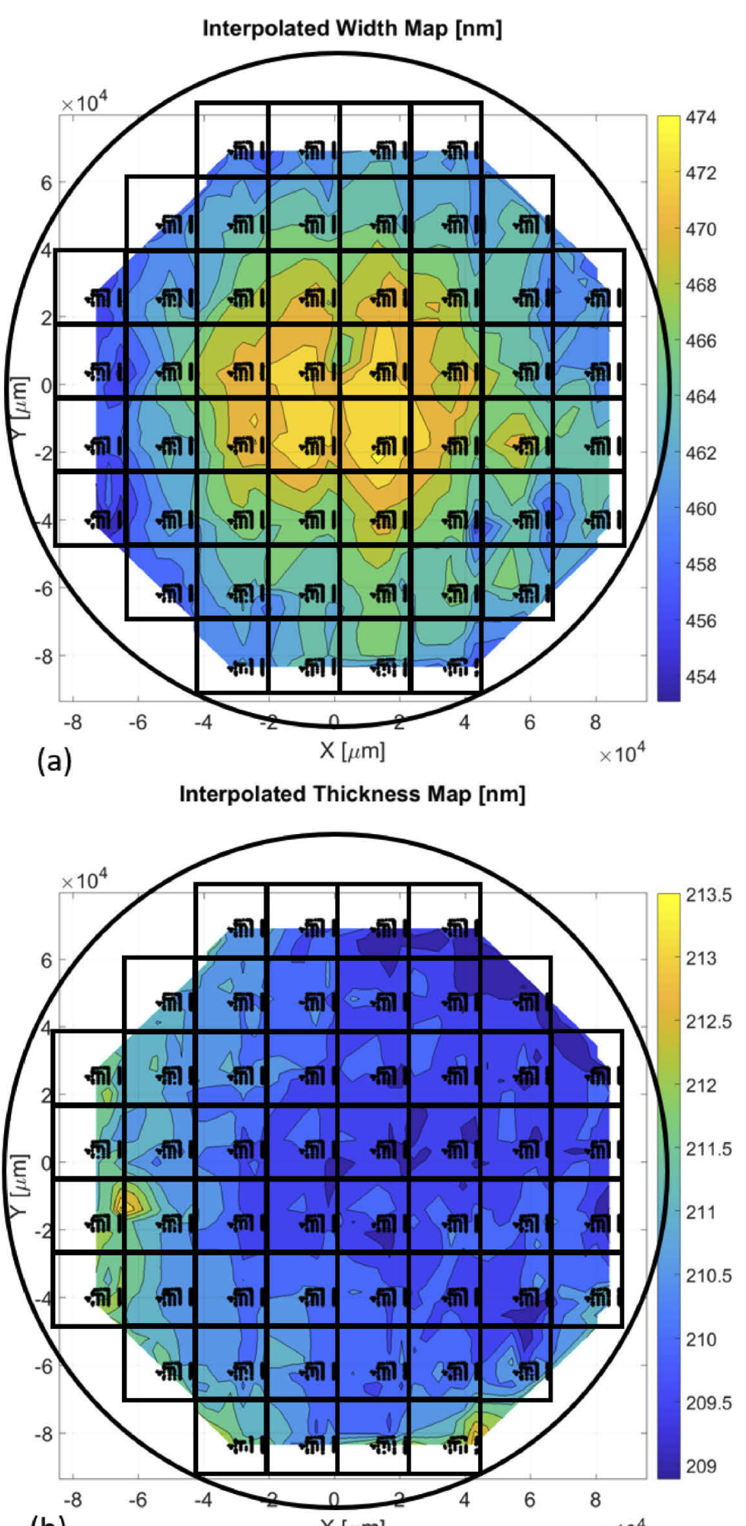

Fig. 5. (a) Interpolated wafer map of (a) linewidth and (b) thickness extracted using the two-stage MZI circuits. 5841 black dots indicate the site of valid samples. Black rectangular grid indicates the boundary of dies. Black circle is the edge of the wafer.

OSA CONTINUUM

and routed to an optical power meter synchronized with the tunable laser. We measured two input-output combinations on each circuit. From each pair of transmission spectra, we first extracted all ten waveguide and DC parameters for each circuit. Then, we interpolated the $n_{eff,1}$ extracted from the lower-order stage to get a reference wafer map of the the effective index n_{eff}. After that, we used this n_{eff} wafer map as a reference at each location of the high-order stage and refined the extraction of the high-order $n_{eff,2}$ values to bracket them in the boundary defined by the local variation. Figure 4(b) presents the extracted effective and group indices of the TE waveguide mode in the high-order stage. We then used the geometry model to map $n_{eff,2}$ and $n_{g,2}$ to width w and thickness t of the high-order MZI arms. The extracted linewidth on the die (X=0, Y=0) in the wafer center ranges from 468.9 nm to 479.5 nm (Fig. 4(c)) and the thickness ranges from 207.6 nm to 209.6 nm (Fig. 4(d)). The standard deviations are 1.9 nm and 0.5 nm, respectively.

After the initial test to extract the die map, we automated the complete wafer-scale measurement for all 52 dies on the wafer. We repeated the procedure for all 6084 samples on the wafer. Some samples are missing one or both optical measurements, which may occur due to unsuccessful alignment in the automated process. Some optical measurements have a bad estimation of the dynamic range which results in saturation in the spectrum. After removing those 'invalid' samples, we got 5841 valid samples (black solid dots in Fig. 5). The derived interpolated wafer map in Fig. 5 is a granular wafer map of the processed silicon photonics wafer. We observe that the linewidth tends to be wider in the center, and it narrows down towards the perimeter of the wafer. The trend of the width variation follows a dome-like shape. The average width is 464.7 nm, where the target value claimed in the technology handbook of the run is 470.0 nm. The measured width has a standard deviation of 4.6 nm. The maximum value on the wafer is 476.0 nm, while the minimum is 450.8 nm. The thickness of the wafer varies like a slope from the South-West to the North-East of the wafer. On the edge of the wafer, the change in thickness reveals some abruptness which may due to the imperfection of the polishing near the wafer perimeter. The average thickness is 210.3 nm where the target value is 215.0 nm. The measured thickness has a standard deviation of 0.8 nm. The maximum extracted thickness on the wafer is 214.3 nm, while the minimum is 208.4 nm.

5. Conclusion

In conclusion, we have designed a compact folded two-stage MZI that can be used to extract fabrication parameters. We applied the Restart-CMA-ES global optimization algorithm to extract multiple parameters of waveguide and DC from only two optical measurements of the circuit. We then mapped the fabricated geometry parameters from the extracted effective and group indices. We derived the die map and wafer map using the design, which proves that the compact device is especially useful for process monitoring and extracting detailed wafer maps for performance evaluation and variability analysis.

Funding

Fonds Wetenschappelijk Onderzoek (G013815N); Agentschap Innoveren en Ondernemen.

Acknowledgments

The authors would like to thank Michael Vanslembrouck for providing the support with automated measurements in cleanroom facilities.

Disclosures

The authors declare no conflicts of interest.

OSA CONTINUUM

References

1. W. A. Zortman, D. C. Trotter, and M. R. Watts, "Silicon photonics manufacturing," Opt. Express **18**(23), 23598 (2010).
2. Y. Xing, J. Dong, U. Khan, and W. Bogaerts, "Hierarchical model for spatial variations of integrated photonics," in *2018 IEEE 15th International Conference on Group IV Photonics (GFP)*, (IEEE, 2018), pp. 1–2.
3. W. Bogaerts, U. Khan, and Y. Xing, "Layout-aware yield prediction of photonic circuits," in *2018 IEEE 15th International Conference on Group IV Photonics (GFP)*, (IEEE, 2018), pp. 1–2.
4. T. W. Weng, D. Melati, A. I. Melloni, and L. Daniel, "Stochastic simulation and robust design optimization of integrated photonic filters," Nanophotonics **6**(1), 299–308 (2017).
5. W. Bogaerts and L. Chrostowski, "Silicon Photonics Circuit Design: Methods, Tools and Challenges," Laser Photonics Rev. **12**(4), 1700237 (2018).
6. S. Selvaraja, W. Bogaerts, P. Dumon, D. Van Thourhout, and R. Baets, "Subnanometer Linewidth Uniformity in Silicon Nanophotonic Waveguide Devices Using CMOS Fabrication Technology," IEEE J. Sel. Top. Quantum Electron. **16**(1), 316–324 (2010).
7. S. Dwivedi, A. Ruocco, M. Vanslembrouck, T. Spuesens, P. Bienstman, P. Dumon, T. Van Vaerenbergh, and W. Bogaerts, "Experimental Extraction of Effective Refractive Index and Thermo-Optic Coefficients of Silicon-on-Insulator Waveguides Using Interferometers," J. Lightwave Technol. **33**(21), 4471–4477 (2015).
8. Z. Lu, J. Jhoja, J. Klein, X. Wang, A. Liu, J. Flueckiger, J. Pond, and L. Chrostowski, "Performance prediction for silicon photonics integrated circuits with layout-dependent correlated manufacturing variability," Opt. Express **25**(9), 9712 (2017).
9. L. Chrostowski, X. Wang, J. Flueckiger, Y. Wu, Y. Wang, and S. T. Fard, "Impact of fabrication non-uniformity on chip-scale silicon photonic integrated circuits," in *Conference on Optical Fiber Communication, Technical Digest Series*, (OSA, 2014), pp. Th2A–37.
10. X. Chen, Z. Li, M. Mohamed, L. Shang, and A. R. Mickelson, "Parameter extraction from fabricated silicon photonic devices," Appl. Opt. **53**(7), 1396 (2014).
11. T. Horikawa, D. Shimura, H. Takahashi, J. Ushida, Y. Sobu, A. Shiina, M. Tokushima, S. H. Jeong, K. Kinoshita, and T. Mogami, "Extraction of SOI thickness deviation based on resonant wavelength analysis for silicon photonics devices," in *2017 IEEE SOI-3D-Subthreshold Microelectronics Technology Unified Conference (S3S)*, (IEEE, 2017).
12. Y. Xing, J. Dong, S. Dwivedi, U. Khan, and W. Bogaerts, "Accurate extraction of fabricated geometry using optical measurement," Photonics Res. **6**(11), 1008 (2018).
13. Y. Xing, U. Khan, A. R. Alves Júnior, and W. Bogaerts, "Behavior model for directional coupler," in *Proceedings Symposium IEEE Photonics Society Benelux*, (2017), pp. 128–131.
14. Y. Li, D. Vermeulen, Y. De Koninck, G. Yurtsever, G. Roelkens, and R. Baets, "Compact grating couplers on silicon-on-insulator with reduced backreflection," Opt. Lett. **37**(21), 4356–4358 (2012).
15. Y. Xing, J. Dong, U. Khan, and W. Bogaerts, "Hierarchical Model for Spatial Variations of Integrated Photonics," in *IEEE International Conference on Group IV Photonics*, (OSA, Cancun, Mexico, 2018).
16. M. Fiers, T. Van Vaerenbergh, K. Caluwaerts, D. Vande Ginste, B. Schrauwen, J. Dambre, and P. Bienstman, "Time-domain and frequency-domain modeling of nonlinear optical components at the circuit-level using a node-based approach," J. Opt. Soc. Am. B **29**(5), 896 (2012).
17. N. Hansen, "The cma evolution strategy: A tutorial," arXiv preprint arXiv:1604.00772 (2016).
18. "The CMA Evolution Strategy," http://cma.gforge.inria.fr/. Accessed: 2019-02-14.
19. A. Auger and N. Hansen, "A restart cma evolution strategy with increasing population size," in *Evolutionary Computation, 2005. The 2005 IEEE Congress on*, vol. 2 (IEEE, 2005), pp. 1769–1776.

178.117.191.172 {ts '2020-02-15 08:49:10'}